IEEE Access
Multidisciplinary | Rapid Review | Open Access Journal

Received September 19, 2020, accepted October 12, 2020, date of publication October 15, 2020, date of current version October 28, 2020.

Digital Object Identifier 10.1109/ACCESS.2020.3031286

Penalized-Likelihood Image Reconstruction for Transmission Computed Tomography Using Adaptive Median Regularization

JI EUN JUNG[1] AND SOO-JIN LEE[2], (Senior Member, IEEE)
[1]Image Processing Group, Genoray Company Ltd., Seongnam 13230, South Korea
[2]Department of Electronic Engineering, Pai Chai University, Daejeon 35345, South Korea

Corresponding author: Soo-Jin Lee (sjlee@pcu.ac.kr)

This work was supported by the National Research Foundation of Korea (NRF) Grant funded by the Korean Government under Grant 2016R1D1A3B04933319.

ABSTRACT Transmission computed tomography (TCT) is a nondestructive imaging technique that provides cross-sectional images from attenuated transmission measurements. In this work we introduce a penalized-likelihood image reconstruction method for TCT where the penalty term takes the form of a median regularizer. More precisely, we develop a center-weighted median regularizer that assigns a variable weight only to the central pixel of each median window so that the fine details can be better preserved. To select an optimal value of the center weight for each median window, we propose an adaptive method that increases the value of the center weight, as the corresponding center pixel is more likely to belong to an edge, and vice versa. The edge-likeliness is measured by the pixel-wise standard deviation (SD), each of whose pixels is transformed into the center weight for the corresponding pixel via the monotonically non-decreasing function derived from the normalized cumulative histogram of the SD image. By noting that the performance of the weighted median regularization is affected by the smoothing parameter that weights the regularization term with respect to the likelihood term, we also propose a similar method to adaptively select the smoothing parameter for each pixel. The experimental results indicate that our proposed method improves not only the overall reconstruction accuracy in terms of the percentage error, but also the contrast recovery coefficients measured in several regions of interest.

INDEX TERMS Transmission computed tomography, image reconstruction, penalized-likelihood methods, median regularization, inverse problems.

I. INTRODUCTION

Transmission computed tomography (TCT), such as X-ray CT, has played a prominent role in medical imaging by providing three-dimensional (3-D) high-resolution anatomical images for diagnostic and therapeutic purposes in various medical disciplines. In the modern TCT scanner, the pair of X-ray source and arc-shaped detector within the system rotates a full 360° around the patient so that the attenuated intensity after the penetration (or the projection) of the X-ray through the body can be measured. To visualize the cross-sectional image of the attenuation coefficient from the given measurements, a mathematical inversion method that can reconstruct an image from attenuated 3-D cone-beam or 2-D fan-beam projections must be used.

The early TCT reconstruction algorithm was based on the analytic method that takes a direct inversion of the forward projections. In this case the path connecting the X-ray source and the detector bin was approximated by a pencil-beam geometry so that the log of the attenuated projections could be expressed as the Radon transform [1], [2]. To reconstruct a cross-sectional image, the discrete version of the inverse Radon transform, also known as the filtered back-projection (FBP) algorithm, has been used over the last decades. Unfortunately, however, the FBP algorithm is known to suffer from its poor image quality with strong streak artifacts smeared back into the image space along the back-projection rays, unless the intensity of the X-ray beam is kept high

The associate editor coordinating the review of this manuscript and approving it for publication was Hengyong Yu.

enough to yield projection data with a high signal-to-noise ratio. To overcome this problem, a different approach using algebraic methods, such as the simultaneous algebraic reconstruction technique (SART) and the simultaneous iterative reconstruction technique (SIRT), was developed for TCT reconstruction, where the data formation process was expressed as a system of linear equations [1], [2] so that the underlying image could be reconstructed by solving the linear equations iteratively. Unfortunately, however, the SART/SIRT and their modified versions [3] still suffer from fundamental limitations in overcoming the ill-posed nature of the reconstruction problem that arises from the sparsity of the measurements in TCT imaging due to the finite projection measurements from the continuous underlying object.

Recently, efforts have been made to reduce the radiation dose in TCT imaging so that the negative risk of cancer from harmful radiation exposures can be reduced. In general, however, as the dose level of radiation decreases, the noise becomes severe in the measurements, which makes the reconstructed image more degraded. To maintain the image quality while allowing the low dose, the (non-deterministic) statistical approach, which provides more accurate solutions by statistically modelling the data acquisition process of imaging systems has been extensively developed over the last decades [4], [5]. The early statistical approach was based on the maximum-likelihood (ML) approach using the expectation maximization [6]. Later, the ML approach was extended to the maximum *a posteriori* (MAP) approach, also known as the penalized-likelihood (PL) approach [7]–[13] by adding suitable regularizers in otherwise unstable ML reconstructions.

Since the PL approach requires repeated computations of time-consuming projection-backprojection operations along with regularization operations, early efforts [14]–[16] have been expended on the development of block-iterative methods that can improve convergence rate. Due to the computational limitation, however, these methods were not as practical as the similar methods developed for emission computed tomography (ECT) whose typical pixel resolution is much lower than that of TCT. Later, with the introduction of high-performance computing techniques using commodity graphics hardware, such as graphics processing units (GPUs), the PL-based methods developed for ECT reconstruction influenced the new developments of the PL-based methods for TCT reconstruction with much higher pixel resolutions [17]–[19].

As the typical underlying image of TCT contains sharp anatomical boundaries formed by different tissues or organs with different attenuation coefficients, most of the PL methods use the convex non-quadratic (CNQ) smoothing penalties developed for ECT reconstruction [20]–[22], where the convexity provides mathematically desirable local and global convergence properties and the non-quadratic form provides edge-preserving smoothing by performing limited smoothing across edges. In recent years, the non-local means approach [23], which was developed for image denoising, has also been widely used in tomographic image reconstruction [24]–[26]. Unlike the conventional local regularization methods, which often smooth out fine structures and details by treating them as noise, the non-local means methods preserve fine structures and details by performing a weighted smoothing process using the self-similarity measured by comparing patch differences. On the other hand, the patch-based regularization methods [27], [28] also take advantage of the self-similarity of an image but preserve edges with the aid of a CNQ penalty rather than with weighted smoothing.

Although the non-local means and patch-based methods usually show several advantages over conventional local regularization methods, any enthusiasm for the use of such methods is tempered by the fact that the computation time significantly increases as the patch size (or the number of pixels within a patch) increases. In addition, the patch-based methods as well as the conventional local regularization methods use CNQ penalties that involve control parameters to adjust the shape of a penalty function. Unfortunately, it is hard to determine the proper value of a control parameter so that true edges can be distinguished from false ones in the presence of noise.

In recent years, there has been increasing interest in developing deep-learning-based methods for medical imaging applications [29]–[31]. For tomographic image reconstruction, however, it has been of a challenging problem to incorporate deep neural networks into the iterative reconstruction framework, which involves repeated projection-backprojection processes. Therefore, most of the deep-learning-based methods have been focused on post-reconstruction corrections. Nevertheless, with the continuing need for the deep learning-based methods, the deep neural network-incorporated iterative tomographic reconstruction methods have great potential to be further developed in the near future.

Independent from the reconstruction methods described above, median-based regularization methods have also been introduced for both emission and transmission reconstructions [32]–[34]. The median-based regularization is attractive in that, unlike conventional smoothing-based regularization methods, where each pixel to be updated is prone to corruption if impulsive noise is present, it preserves edges as well as locally monotonic regions by imposing the behavior that each pixel is attracted to its local median and is thereby less affected by impulsive noise.

The early median prior model developed for iterative tomographic reconstruction, namely the median-root prior (MRP) reported in [32], [33], was based on a heuristic empirical method using a kind of one-step-late (OSL) algorithm [20] which is not derivable form an objective function. Since the convergence of the OSL algorithm is not guaranteed, any reconstruction method using the OSL algorithm, which includes the MRP algorithm, can diverge for relatively large values of the smoothing parameter. Moreover, the local median in the MRP algorithm is obtained by the median

operation within the window at each iteration, rather than it is obtained by optimizing an objective function, which makes the resulting algorithm unanalyzable. Later, Hsiao *et al.* [34], proposed a new convex median prior for emission tomography reconstruction and showed that the median regularization could be formulated within a PL context.

In this work we generalize the median prior originally developed for ECT in [34] and re-derive the PL reconstruction algorithm dedicated to TCT. A similar attempt to use the median prior in TCT reconstruction was reported in [35]. However, it simply converts the inverse problem of transmission imaging to that of emission imaging by taking the log of the projection measurements and directly uses the method in [34], which is dedicated to ECT. Unfortunately, due to the non-linear transform of the log of the attenuated transmission data, it does not preserve the statistical character of the measured data and therefore is not regarded as a statistical reconstruction method dedicated to TCT. In contrast, our new method derives a statistical TCT reconstruction algorithm without transforming the measured data prior to the reconstruction process.

Besides the re-derivation of the PL algorithm with the median regularizer for TCT reconstruction, a major improvement considered in this work is to use the center-weighted median regularization. In the formulation of our reconstruction algorithm, the penalty for the prior is expressed as a convex function and involves a weight for the center element of the median window [36]–[38]. The center-weighted median regularization in this case allows the center element in each median window to be more probable to become a median so that the regularization process can better restore fine details by avoiding a typical problem of the conventional median regularization that often eliminates any structure that occupies less than half of the window elements. (Similar works using weighted median filtering for non-tomographic applications can be found in [36]–[43].)

In this work we propose a novel method to adaptively choose the optimal value of the center weight for each pixel by using a nonlinear mapping function derived from the previous estimate of the underlying image. We also investigate the effect of the smoothing parameter in the weighted median regularization and finally propose a similar method of choosing the optimal value of the smoothing parameter for each pixel as well so that both of the two closely-related parameters can be adaptively chosen.

II. PENALIZED-LIKELIHOOD APPROACH TO TCT RECONSTRUCTION

We first define our notations to explain the geometry of a typical TCT scanner shown in Fig. 1. In TCT reconstruction, the parameters to be estimated are the attenuation coefficients $\boldsymbol{\mu}$ of an underlying object from the transmission measurements $\mathbf{y}$. In this article, the vectors $\boldsymbol{\mu}$ and $\mathbf{y}$ are lexicographically ordered so that μ_j represents the $j(x, y)$-th pixel of the underlying image $\boldsymbol{\mu} = \{\mu_j | j = 0, \ldots, J-1\}$ in the 2-D space and y_i represents the $i(t, \theta + \alpha)$-th measurement of the

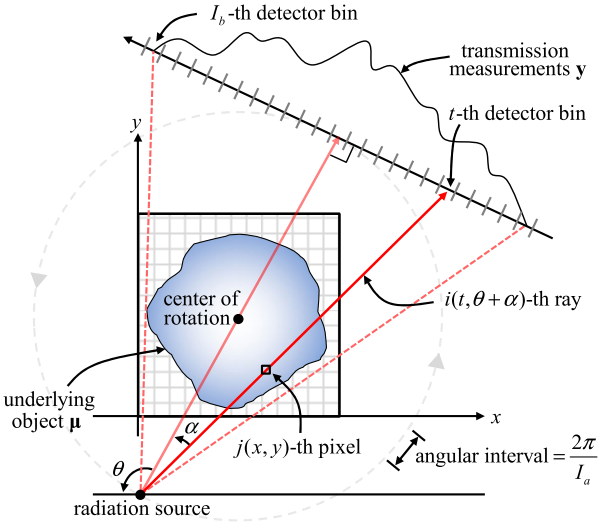

FIGURE 1. Schematic geometry of fan-beam projection for TCT.

observed transmission data $\mathbf{y} = \{y_i | i = 0, \ldots, I-1\}$ in the 2-D space of $I_a \times I_b$, where I_a is the number of discrete angles and I_b is the number of elements (or bins) in the detector array. (See Fig. 1 for t, θ and α.) Fig. 1 shows a schematic geometry of the fan-beam projection used in this work, where the detector array consisting of I_b elements rotates about the center of rotation, over 360° discretized into I_a angles.

The transmission measurement of the i-th ray denoted as y_i is independent and identically Poisson distributed with mean $\bar{y}_i$ as follows:

$$y_i \sim Poisson\{\bar{y}_i\}, \quad \text{where } \bar{y}_i = b_i e^{-[\mathbf{A}\boldsymbol{\mu}]_i} + r_i. \tag{1}$$

In (1), b_i denotes the blank scan counts (generated from the radiation source) of the i-th ray, r_i is the mean of the background events, and $\mathbf{A}$ is the system matrix whose element a_{ij} represents the contribution of the attenuation coefficient μ_j in the j-th pixel to the i-th ray. The term $[\mathbf{A}\boldsymbol{\mu}]_i = \sum_j a_{ij}\mu_j$ indicates the projection of the underlying object through the i-th ray.

The PL approach to TCT reconstruction is then to estimate attenuation coefficients $\boldsymbol{\mu}$ using the following minimization:

$$\hat{\boldsymbol{\mu}} = \arg\min_{\boldsymbol{\mu}} \left[-L(\mathbf{y}|\boldsymbol{\mu}) + \lambda R(\boldsymbol{\mu})\right], \tag{2}$$

where $L(\mathbf{y}|\boldsymbol{\mu})$ is the log-likelihood, $R(\boldsymbol{\mu})$ is the regularizer (also known as the prior) and λ is a smoothing parameter that weights the regularization term relative to the likelihood term. The negative log-likelihood, after eliminating constant terms, is given by

$$-L(\mathbf{y}|\boldsymbol{\mu}) = \sum_i \left[\bar{y}_i - y_i \log(\bar{y}_i)\right] = \sum_i \varphi_i([\mathbf{A}\boldsymbol{\mu}]_i),$$
$$\text{where } \varphi_i(l) = (b_i e^{-l} + r_i) - y_i \log(b_i e^{-l} + r_i). \tag{3}$$

The regularizer is usually modeled as a penalty function that forces each pixel in the reconstructed image to be similar

to its neighbors so that irregular pixels due to noise can be regularized. In this work, instead of using the conventional edge-preserving CNQ penalties determined by measuring the distance between the pixel to be updated and its neighbors, we use different penalty function designed for median regularization. The mathematical formulation of the median regularizer is described in the following section.

III. METHODS

A. MEDIAN REGULARIZATION FOR TCT RECONSTRUCTION

The penalty function for median regularization is given by [34]

$$R(\boldsymbol{\mu}, \mathbf{m}) = \sum_{j} \sum_{j' \in N_j} \omega_{jj'} \left| \mu_j - m_{j'} \right|, \tag{4}$$

where $\mathbf{m}$ is the auxiliary vector whose j'-th component $m_{j'}$ is in register with μ_j, N_j represents the local neighborhood system of the pixel located at j including j itself, $\omega_{jj'}$ represents the weight between μ_j and $\{m_{j'}; j' \in N_j\}$. Note that, while the conventional edge-preserving CNQ penalty function usually penalizes the neighboring pixels' difference, $\mu_j - \mu_{j'}$, by decreasing the increment of the penalty for a relatively large pixels' difference, the penalty function for median regularization penalizes the difference between μ_j and $m_{j'}$. (The details on the role of the auxiliary variable $\mathbf{m}$ and the proof of convexity of the form in (4) can be found in [34].) Since the regularization term in (4) depends on the two variables $\boldsymbol{\mu}$ and $\mathbf{m}$, the PL approach described in (2) must be modified to the form of a joint minimization over the two variables. When $\omega_{jj'} = 1$ optimizing (4) leads to the local median. For example, finding the value of μ_j by minimizing $\sum_{j' \in N_j} \left| \mu_j - m_{j'} \right|$ leads the local median of $m_{j'}$'s. Since the PL approach described in (2) will be modified to a joint minimization problem over both $\boldsymbol{\mu}$ and $\mathbf{m}$, $m_{j'}$'s also become themselves local medians of μ_j's within the new alternating minimization procedure. In this work, since the penalty term involving the absolute value (4) is non-differentiable, the penalty function of absolute value, $\psi(\xi) = |\xi|$, is approximated as follows [34]:

$$\psi(\xi) = \lim_{\varepsilon \to 0} \sqrt{\xi^2 + \varepsilon} \tag{5}$$

When positive weights are assigned independently to $\omega_{jj'}$ for $j' \in N_j$, (4) is generalized to the weighted median regularization (WMR). To understand the behavior of WMR in (4), readers may refer to the interpretation of weighted median in the aspect of least absolute regression [44], where the weighted median of $\{m_{j'}; j' \in N(j)\}$, for example, is represented by

$$\text{MED}\left\{\omega_{jj'} \diamond m_{j'}; j' \in N(j)\right\}. \tag{6}$$

In (6) MED $\{\cdot\}$ is the median operation and $\diamond$ denotes duplication. For example, $\omega \diamond \varsigma = \overbrace{\varsigma, \ldots, \varsigma}^{\omega-\text{times}}$. Although WMR in (4) is conceptually related to (6), it cannot be represented by (6), and the value of $\omega_{jj'}$ in (4) is not limited to a positive integer.

With the WMR that involves the two variables $\boldsymbol{\mu}$ and $\mathbf{m}$, the PL approach in (2) is modified as the following minimization problem of a joint objective $\Phi(\boldsymbol{\mu}, \mathbf{m})$:

$$\hat{\boldsymbol{\mu}}, \hat{\mathbf{m}} = \arg\min_{\boldsymbol{\mu}, \mathbf{m}} \left[\Phi(\boldsymbol{\mu}, \mathbf{m})\right], \quad \text{where} \quad \Phi(\boldsymbol{\mu}, \mathbf{m}) = -L(\mathbf{y}|\boldsymbol{\mu}) + \lambda R(\boldsymbol{\mu}, \mathbf{m}). \tag{7}$$

To solve the above joint minimization problem, the following alternating iterative algorithm is used [34]:

$$\hat{\boldsymbol{\mu}}^{n+1} = \arg\min_{\boldsymbol{\mu}} \left[\Phi(\boldsymbol{\mu}, \hat{\mathbf{m}}^n)\right], \tag{8}$$

$$\hat{\mathbf{m}}^{n+1} = \arg\min_{\mathbf{m}} \left[R(\hat{\boldsymbol{\mu}}^{n+1}, \mathbf{m})\right]. \tag{9}$$

The actual minimizations in both (8) and (9) are performed by iterative procedures. The details on the iterative procedure for each minimization will be described in Sec. III. C.

B. ADAPTIVELY SELECTING FREE PARAMETERS FOR WEIGHTED MEDIAN REGULARIZATION

In this work we adopt a special case of weighted median filters, namely the center weighted median filter [36]–[38], which assigns non-unity weight $w_{jj'}$ to the center pixel of the median window while setting all other pixels to one. The center weighted median filter is performed by multiply duplicating the center pixels so that the center pixel and its duplicated pixels become as many as the value of the center weight. When non-integer real positive weights are used, the filter operation can be performed by sorting the elements in the median window from the largest to the smallest and choosing the element whose accumulated weights from the largest element just exceeds half of the total sum of weights [39].

Ko and Lee [36] showed assigning higher weight to the center pixel within the window can accurately preserve the image detail including step edges and lines while reducing the noise when they are corrupted by Gaussian noise. However, as the center weight increases beyond a certain level, the resulting image starts to deteriorate. In fact, as the center weight increases, the weighted median regularization defined in (4) tends to increase the roughness in monotonic regions while enhancing the edges, which implies that when the center pixel is corrupted by noise, it is less probable to be replaced by an uncorrupted pixel due to its high weight. To solve this problem, the center weight needs to be selectively chosen to keep low values in monotonic regions and high values at edges.

In this work we use an adaptive method of choosing the center weight in accordance with the pixel-wise roughness measured by calculating the standard deviation (SD) image defined as follows:

$$s_j^n = \sqrt{\frac{1}{N-1} \sum_{k \in \mathbf{W}_j} \left[\hat{\mu}_k^n - \left(\frac{1}{N} \sum_{j' \in \mathbf{W}_j} \hat{\mu}_{j'}^n \right) \right]^2}, \quad \forall j, \tag{10}$$

where s_j^n is the j-th pixel in the SD image $\mathbf{s}^n \in \{s_j^n; j = 0, \ldots, J-1\}$ calculated within the 3×3 window $\mathbf{W}_j$ centerd at j in the previous (the n-th) estimate $\hat{\boldsymbol{\mu}}^n$and $N = 9$ in this case.

In order to select the center weight with the aid of the SD image, one can consider directly using the SD image so that each pixel value of the SD image can be linearly transformed into a center weight for WMR. However, a typical SD image usually exhibits meaningfully high SD values only for the coarse-scale edges with relatively high contrast. Therefore, using the SD image may ignore fine-scale edges with relatively low contrast. To overcome this problem, instead of directly using the SD image, we propose to use a cumulative histogram of the SD image. Our motivation of using the cumulative histogram lies in our notion that it can not only reflect the roughness determined from the SD image, but also provide a more suitable transform that can boost up the value of the center weight so that the fine-scale edges with low contrast can be better preserved. Transforming the SD image into the center weight is performed by the following procedure: (i) compute the histogram of the SD image $\mathbf{s}^n$ at the n-th PL iteration; (ii) calculate the normalized cumulative histogram (NCH); (iii) for each pixel of the current estimate $\hat{\mu}_j^{n+1}$, refer to the corresponding pixel value s_j^n in the SD image and transform it into the center weight via the NCH curve.

The use of the NCH curve can also be viewed as equalizing the histogram of the SD image. Note that the histogram equalization process is usually performed by transforming the pixel intensities via a mapping function (also known as a look-up table) generated by accumulating the histogram. The motivation for this transformation comes from treating the pixel intensity as a random variable. Suppose that we transform a random variable X, whose probability density function $\Pr(X = x) = f_X(x)$ is known, into a new random variable $V = g(X)$. If the function $v = g(x)$ has a unique inverse and its real root is x_1, the new probability density function is given by

$$\Pr(V = v) = f_V(v) = \frac{f_X(x_1)}{|g'(x_1)|}. \tag{11}$$

If the function for the transformation is given by $g(x) = \Pr(X \leq x)$, which is the probability distribution of X, the probability density function of the new random variable V in (11) becomes uniform. Therefore, transforming the SD image via the NCH curve is equivalent to equalizing the histogram of the SD image. In our case, using the histogram-equalized SD image has the effect of spreading out the most frequent SD values so that the areas of low median weights can gain high values enough to preserve fine-scale edges with low contrast.

The cumulative histogram $\mathrm{H}^n(\tau)$ of the SD image at the n-th iteration $\mathbf{s}^n$ can be calculated by

$$\mathrm{H}^n(\tau) = \sum_{k=0}^{\tau} \mathrm{h}^n(k), \tag{12}$$

where $\mathrm{h}^n(\cdot)$ is the histogram of $\mathbf{s}^n$ and τ is the quantized SD value. The center weight for the j-th pixel at the n-th iteration ω_{jj}^n is then given by

$$\omega_{jj}^n = \Gamma_\omega^n(s_j), \quad \text{where } \Gamma_\omega^n(\tau) = 1 + \frac{(u_{\mathbf{W}} - 1)\mathrm{H}^n(\tau)}{\mathrm{H}^n(T)}. \tag{13}$$

In (13) $\Gamma_\omega^n(\tau)$ is the NCH of the SD image at the n-th iteration, T is the maximum value of τ and $u_{\mathbf{W}}$ is the maximum value of the center weight. Note that the range of $\Gamma_\omega^n(\tau)$ is now $[1, u_{\mathbf{W}}]$. We call this method the adaptive WMR (AWMR).

In general, the performance of a PL-based method is strongly affected by the smoothing parameter λ that weights the regularization term with respect to the likelihood term. Larger smoothing parameter may overweight the strength of regularization. When the regularizer is modeled by a simple quadratic form, large values of the smoothing parameter result in oversmoothed images whose edges and fine details are blurred. According to our own observation, when the regularizer is modeled as a center-weighted median operation, the effect of increasing the smoothing parameter λ is similar to that of decreasing the median center weight, and vice versa. While various methods [45]–[49] of selecting the smoothing parameter (or the regularization parameter) have been proposed, each method is suitable only for a specific regularizer. Therefore, a parameter selected for a specific regularizer may not work for other regularizers [49].

In this work, to find the optimal value of λ for a given center weight, we attempt to adaptively adjustλ using the roughness information obtained from the SD image as done for the AWMR. The only difference in employing the NCH curve for λ compared to that for the center weight is to use the monotonically decreasing character of the transformation as opposed to the monotonically increasing character for the median center weight. To design a monotonically decreasing function by using the NCH curve, we first flip the NCH curve with respect to the abscissa (the τ axis) and shift it in the ordinate by the maximum value of NCH. In this case the value of the smoothing parameter λ_j^{n+1} for the current estimate $\hat{\mu}_j^{n+1}$ is given by:

$$\lambda_j^{n+1} = \alpha \left\{ \Gamma_\lambda^n(T) - \Gamma_\lambda^n(\tau) \right\} \big|_{\tau = s_j},$$
$$\text{where} \quad \Gamma_\lambda^n(\tau) = \frac{2\eta \mathrm{H}^n(\tau)}{\mathrm{H}^n(T)} + (1 - \eta). \tag{14}$$

In (14) α is an initial guess of λ_j^{n+1} and $\eta \in [0, 1]$. Hence the value of λ_j^{n+1} is determined within the range of $[\alpha(1-\eta), \alpha(1+\eta)]$ centered at α.

C. OPTIMIZATION METHOD

To optimize the penalized-likelihood objective for TCT reconstruction, a variety of different methods [8], [15], [50]–[52] have been proposed. For our reconstruction problem described in (7), we employ the method of optimization transfer using separable paraboloidal surrogates (SPS) [15], which transforms the complex objective function into simpler quadratic surrogate functions that are convergent to

the original objective function. In this case, the quadratic optimization is performed for the surrogate function in place of the original function at each iteration. To increase the convergence rate of the algorithm, a block-iterative method, such as the well-known ordered subsets (OS) method [53], can be used. The OS method subdivides the observed data into several subsets (or blocks) and then progressively processes each subset of the data by performing projection and back-projection operations at each iteration. While the OS-based methods have been very popular in tomographic reconstruction, they usually do not converge to the optimal solution. In this work, we also apply the OS principle to our reconstruction algorithm but employ the improved version of the paraboloidal surrogates method, namely the transmission incremental optimization transfer (TRIOT) algorithm [50], which is not only faster than the SPS algorithm and even its accelerated version by the OS method, but also guaranteed to converge to the optimal solution.

To apply the OS principle, we first partition the objective function $\Phi(\boldsymbol{\mu}, \hat{\mathbf{m}}^n)$ into a set of the P angular subsets as follows:

$$\Phi(\boldsymbol{\mu}, \hat{\mathbf{m}}^n) = \sum_p \Phi_p\left(\boldsymbol{\mu}, \hat{\mathbf{m}}^{n,p}\right),$$

$$\text{where} \quad \Phi_p\left(\boldsymbol{\mu}, \hat{\mathbf{m}}^{n,p}\right) = \left\{ \sum_{i \in S(p)} \varphi_i\left([\mathbf{A}\boldsymbol{\mu}]_i\right) \right\} + \frac{\boldsymbol{\lambda}^n}{P} R\left(\boldsymbol{\mu}, \hat{\mathbf{m}}^{n,p}\right). \tag{15}$$

In (15) $S(p) \in \{S(p); p = 0, \ldots, P-1\}$ is the p-th angular subset. In the TRIOT algorithm, the quadratic surrogates, $\phi_p(\boldsymbol{\mu}; \hat{\boldsymbol{\mu}}^n, \hat{\mathbf{m}}^{n,p})$, which are tangent to the original subobjective function $\Phi_p(\boldsymbol{\mu}, \hat{\mathbf{m}}^n)$ at the current estimate, are used in place of $\Phi_p(\boldsymbol{\mu}, \hat{\mathbf{m}}^n)$ so that the minimization problem becomes a simple quadratic optimization problem. In addition, for the global convergence, the following augmented function is minimized at each iteration:

$$F(\boldsymbol{\mu}; (\hat{\boldsymbol{\mu}}^{n,0}, \ldots, \hat{\boldsymbol{\mu}}^{n,P-1}), \hat{\mathbf{m}}^{n,p}) = \sum_{v=0}^{P-1} \phi_v(\boldsymbol{\mu}; \hat{\boldsymbol{\mu}}^n, \hat{\mathbf{m}}^{n,p}) \geq \Phi(\boldsymbol{\mu}, \hat{\mathbf{m}}^n). \tag{16}$$

The above augmented function is expressed as the following separable quadratic surrogates [15]:

$$\phi_p(\boldsymbol{\mu}; \hat{\boldsymbol{\mu}}^n, \hat{\mathbf{m}}^{n,p}) = \Phi_p(\hat{\boldsymbol{\mu}}^n, \hat{\mathbf{m}}^{n,p}) + \nabla\Phi_p(\hat{\boldsymbol{\mu}}^n, \hat{\mathbf{m}}^{n,p})(\boldsymbol{\mu} - \hat{\boldsymbol{\mu}}^n) + \frac{1}{2}\breve{c}_{pj}(\hat{\boldsymbol{\mu}}^n, \hat{\mathbf{m}}^{n,p})(\boldsymbol{\mu} - \hat{\boldsymbol{\mu}}^n)^2, \tag{17}$$

where ∇ denotes the partial derivative with respect to μ_j and $\breve{c}_{pj}$ is the curvature term of ϕ_p, which is given by

$$\breve{c}_{pj}(\boldsymbol{\mu}, \hat{\mathbf{m}}^{n,p}) = \sum_{i \in S(p)} a_{ij}\gamma_i c_i([\mathbf{A}\boldsymbol{\mu}]_i) + \frac{2\lambda_j^n}{P} \sum_{j' \in N_j} \varpi_\psi(\mu_j - \hat{m}_{j'}^{n,p}), \tag{18}$$

where $\gamma_i = \sum_{j'} a_{ij'}$ is for the decoupling problem [54]. For the derivation of the surrogates for $\Phi_p(\boldsymbol{\mu}, \hat{\mathbf{m}}^n)$, the surrogates for the likelihood and the regularization terms are constructed separately. Here, c_i and $\varpi_\psi(\xi) = \nabla\psi(\xi)/\xi$ represent the curvatures of the surrogates for the likelihood and the regularization terms, respectively. In this work, we use the optimum curvature for the likelihood term, which provides the fastest convergence rate while sustaining monotonicity [15].

The final update equation for $\boldsymbol{\mu}$ derived from (17) is given by

$$\hat{\mu}_j^{n,p+1} = \sum_p \left\{ \hat{\mu}_j^{n,p} \breve{c}_{pj}(\boldsymbol{\mu}, \hat{\mathbf{m}}^{n,p}) - \left[\sum_{i \in S(p)} a_{ij} \nabla\varphi_i([\mathbf{A}\hat{\boldsymbol{\mu}}^{n,p}]_i) + \frac{\lambda_j^n}{P} \sum_{j' \in N_j} \nabla\psi(\hat{\mu}_j^{n,p} - \hat{m}_{j'}^{n,p}) \right] \right\} \Big/ \sum_p \breve{c}_{pj}(\boldsymbol{\mu}, \hat{\mathbf{m}}^{n,p}), \quad \forall j, \tag{19}$$

where $\hat{\mu}_j^{n,p}$ represents the j-th pixel value of $\boldsymbol{\mu}$ estimated from the p-th angular subset at the n-th iteration. Since one iteration is completed after computations for all the subsets $\{S(p); p = 0, \ldots, P-1\}$ are done, the final update at the n-th iteration is assigned as $\hat{\boldsymbol{\mu}}^n = \hat{\boldsymbol{\mu}}^{n,P-1}$, where $\hat{\boldsymbol{\mu}}^n$ is the estimate at the end of the n-th iteration, which is equal to the estimate after all P projection views are processed. In this work, as suggested in [53] for further accelerations, we performed a few iterations of the ordered-subsets separable paraboloidal surrogates (OS-SPS) algorithm in initial iterations. (Since the OS-SPS algorithm is not guaranteed to converge, it is used here in initial iterations only.)

To achieve the alternating iterative algorithm described in (8) and (9), the minimization of the regularization term with respect to the auxiliary variable $\mathbf{m}$ in (9) is performed by subiterations of the SPS [15] method so that the local median is obtained. Given $\hat{\boldsymbol{\mu}}^{n,p}$, the update equation for $\mathbf{m}$ is given by

$$\hat{m}_{j'}^{n,p+1,l+1} = \frac{\sum_j \omega_{jj'}^n \frac{(\hat{\mu}_j^{n,p+1} + \hat{m}_{j'}^{n,p+1,l})}{\psi(\hat{\mu}_j^{n,p+1} - \hat{m}_{j'}^{n,p+1,l})}}{2\sum_j \frac{\omega_{jj'}^n}{\psi(\hat{\mu}_j^{n,p+1} - \hat{m}_{j'}^{n,p+1,l})}}, \quad \forall j' \in N_j, \tag{20}$$

where $l \in \{l | 0, \ldots, L-1\}$ is the index for the subiteration. Note that the finally updated value at the $(L-1)$-th iteration is assigned as $\hat{\mathbf{m}}^{n,p} = \hat{\mathbf{m}}^{n,p,L-1}$, where $\hat{\mathbf{m}}^{n,p}$ is the estimate at the end of the n-th iteration after processing L subiterations.

Table 1 shows the outline for the PL algorithm using AWMR with adaptive smoothing (hereafter referred to as AWMR-AS), where $\breve{c}_{pj}(\boldsymbol{\mu}, \hat{\mathbf{m}})$ is the curvature defined in (18) and $\nabla\Phi_p(\hat{\boldsymbol{\mu}}, \hat{\mathbf{m}})$ is the partial derivative of the partitioned objective function for the p-th angular subset described in (15). For the PL algorithm using AWMR only, the smoothing parameter λ is fixed with a manually chosen value. For the PL algorithm using WMR with adaptive smoothing (hereafter referred to as WMR-AS), the center weight ω is fixed with a manually chosen value.

While the PL algorithm with the standard median regularizer derived in this work is guaranteed to converge, the

TABLE 1. Outline for PL algorithm using AWMR-AS.

Initialize $\hat{\boldsymbol{\mu}} = \hat{\boldsymbol{\mu}}^0$, $\hat{\mathbf{m}} = \hat{\mathbf{m}}^0$, $\alpha = \alpha^0$, $\omega = 1$;
Calculate SD image $\mathbf{s}$;
for each iteration $n \in \{n \mid 0,\ldots,N-1\}$
  for each subset $p \in \{p \mid 0,\ldots,P-1\}$ // TRIOT update for $\hat{\boldsymbol{\mu}}$
    for each pixel $j \in \{j \mid 0,\ldots,J-1\}$
      $\lambda_j = \alpha\{\Gamma_\lambda(T) - \Gamma_\lambda(s_j)\}$;
      Compute curvature $\breve{c}_{pj}(\boldsymbol{\mu}, \hat{\mathbf{m}})$;
      Compute $\nabla\Phi_p(\hat{\boldsymbol{\mu}}, \hat{\mathbf{m}})$;
      Update $\hat{\mu}_j = \dfrac{\sum_p \hat{\mu}_j \breve{c}_{pj}(\boldsymbol{\mu}, \hat{\mathbf{m}}) + \nabla\Phi_p(\hat{\boldsymbol{\mu}}, \hat{\mathbf{m}})}{\sum_p \breve{c}_{pj}(\boldsymbol{\mu}, \hat{\mathbf{m}})}$;
    end
    Update SD image $\mathbf{s}$;
    for each pixel $j \in \{j \mid 0,\ldots,J-1\}$
      $\omega_{jj} = \Gamma_\omega(s_j)$;
      for each subiteration $l \in \{l \mid 0,\ldots,L-1\}$ // SPS update for $\hat{\mathbf{m}}$
        Update $\hat{m}_{j'} = \dfrac{\sum_j \dfrac{\omega_{jj'}(\hat{\mu}_j + \hat{m}_{j'})}{\sqrt{(\hat{\mu}_j - \hat{m}_{j'})^2 + \varepsilon}}}{2\sum_j \dfrac{\omega_{jj'}}{\sqrt{(\hat{\mu}_j - \hat{m}_{j'})^2 + \varepsilon}}}, \forall j' \in N_j$;
      end
    end
  end
end

adaptive versions, such as AWMR, AWMR-AS and WMR-AS, are not provably convergent. According to our own observations, however, the convergence behaviors of the objective versus iterations were almost indistinguishable between the non-adaptive version and the adaptive version. In addition, the results of the adaptive methods were not affected by the initial states.

IV. SIMULATIONS AND RESULTS

To evaluate the performance of our proposed method, we performed the 2-D simulation studies using the extended cardiac-torso (XCAT) software phantom (version 2) [55] consisting of 256 × 256 square pixels with the 2.3mm width as shown in Fig. 2(a), which provides a virtual model of the patient's anatomy. (The phantom image is regarded as the true underlying image whose pixel values indicating the attenuation coefficients are generated as if they were from a live patient.) The transmission data were acquired from the fan-beam projector with 430 detector bins (I_b in Fig. 1), each of which is 1.37mm long, and 480 discrete angles (I_a in Fig. 1) over 360°. To evaluate our proposed methods quantitatively, we generated 50 independent Poisson noise trials of the transmission data and reconstructed 50 images for each reconstruction method. A sample of the simulated data using the phantom in Fig. 2(a) is shown in Fig. 2(b), where the total number of counts is approximately 1.7×10^6 excluding the blank counts. Fig. 2(c) shows a typical noise level when the image is reconstructed by the conventional FBP method.

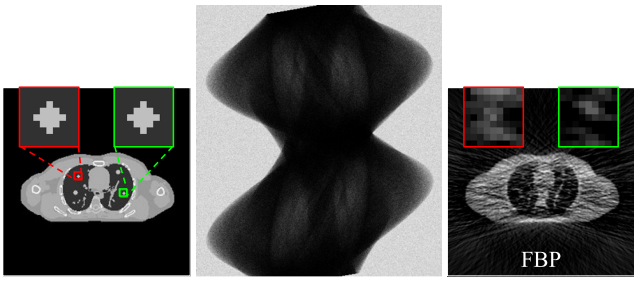

FIGURE 2. Illustration of conventional FBP reconstruction using 2-D software phantom, (a) 256 × 256 XCAT software phantom, (b) 430 × 480 noisy transmission data, (c) FBP reconstruction from the data in (b).

To compare the proposed PL reconstruction method using WMR with other existing methods, we first show ML and PL reconstructions using the conventional regularizers, such as quadratic (QD) and CNQ regularizers. For the CNQ regularizer, we used the penalty function defined as $\psi(\xi) = \delta^2\left[|\xi/\delta| - \log(1 + |\xi/\delta|)\right]$ with $\delta > 0$ [20]. Figs. 3(a) and (b) show ML reconstructions using the ordered subsets convex (hereafter referred to as ML-OSC) algorithm [14] with 32 subsets stopped at the 10-th iteration and 20-th iteration, respectively. (The percentage error (PE) used for the accuracy measure of each reconstruction is defined as $PE = \left\|(\boldsymbol{\mu} - \hat{\boldsymbol{\mu}})/\boldsymbol{\mu}\right\|_2 \times 100\%$, where $\boldsymbol{\mu}$ is the phantom image, and $\hat{\boldsymbol{\mu}}$ is the reconstructed image.) Figs. 3(c) and (d) show the PL reconstructions using the QD regularizer with $\lambda = 10^4$ and $\lambda = 10^5$, respectively. Figs. 3(e), (f) and (g) show the PL reconstructions using the CNQ regularizer with $\lambda = 10^5$ and three different values of δ (10^{-4}, 3×10^{-4}, and 9×10^{-4}, respectively). For the PL reconstructions performed in our simulations, to achieve faster convergence, each algorithm was performed by 2 iterations of OS-SPS followed by 18 iterations of TRIOT with 32 subsets. (In this case, considering the 32 subsets used in each algorithm, the effective number of iterations for OS-SPS and TRIOT was 64 and 576, respectively.)

According the ML-OSC reconstructions shown in Figs. 3(a) and (b), as the number of iterations increases, the noise level also increases because the ML algorithm tries to reconstruct the image which most agrees with the contaminated measurements by maximizing the likelihood term. For the PL algorithm using the QD regularizer (hereafter referred to as PL-QD), whose results are shown in Figs. 3(c) and (d), while the noise is smoothed out as the smoothing parameter λ increases, the edges tend to be oversmoothed as clearly shown in Fig. 3(d). On the other hand, the PL algorithm using the CNQ regularizer (hereafter referred to as PL-CNQ), whose results are shown in Figs. 3(e), (f) and (g), can not only suppress the noise in the monotonic regions, but preserve the edges, thereby improving the overall reconstruction accuracy. Unfortunately, however, the performance of the PL-CNQ algorithm depends highly on the choice of the additional parameter δ for a given value of the smoothing parameter λ as illustrated in Fig. 3(e) and (g).

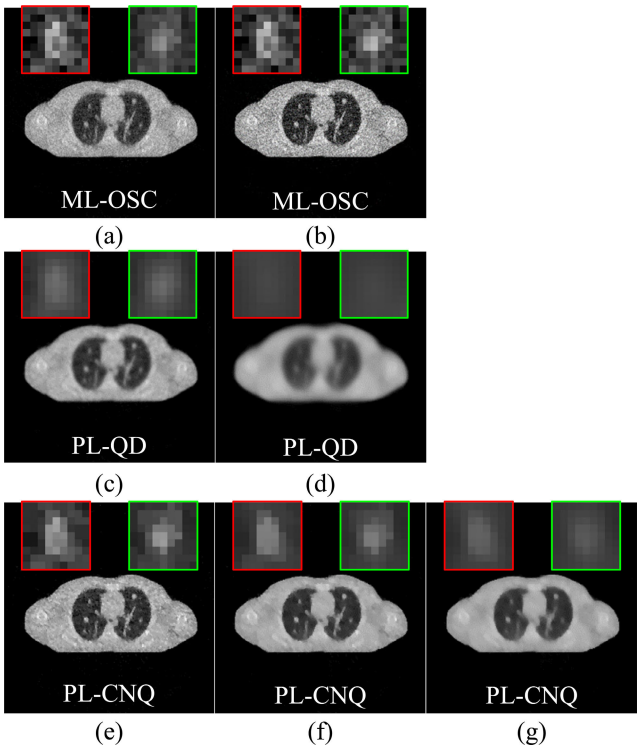

FIGURE 3. Anecdotal ML-OSC and PL-QD/CNQ reconstructions from the transmission data shown in Fig. 2(b) (All of the algorithms were accelerated by using 32 ordered subsets. The number of iterations used for ML is either 10 or 20 and that for PL is 20.), (a) ML-OSC with 10 iterations (PE = 17.694%), (b) ML-OSC with 20 iterations (PE = 21.350%), (c) PL-QD with $\lambda = 10^4$ (PE = 17.787%), (d) PL-QD with $\lambda = 10^5$ (PE = 23.666%), (e) PL-CNQ with $\lambda = 10^5$ and $\delta = 10^{-4}$ (PE = 15.403%), (f) PL-CNQ with $\lambda = 10^5$ and $\delta = 3 \times 10^{-4}$ (PE = 14.418%), (g) $\lambda = 10^5$ and $\delta = 9 \times 10^{-4}$ (PE = 16.019%).

To test our ideas of using WMR for PL reconstruction, we compared the performances of the following four median-based regularizers: (i) WMR, (ii) AWMR, (iii) WMR-AS and (iv) AWMR-AS, where each algorithm was first performed by 2 iterations of OS-SPS followed by 18 iterations of TRIOT with 32 subsets for further acceleration of the convergence in estimating $\boldsymbol{\mu}$ (after 5 subiterations of the SPS method to estimate $\mathbf{m}$).

First, we attempted to find an optimal pair of the smoothing parameter λ and center weight ω for WMR by examining the reconstruction accuracy in terms of the mean of percentage error (MPE) evaluated over K (set to 50 in this simulation) noise trials as follows:

$$MPE = \frac{1}{K} \sum_k \sqrt{\sum_j \left(\frac{\mu_j - \hat{\mu}_j^k}{\mu_j} \right)^2} \times 100\%, \qquad (21)$$

where μ_j and $\hat{\mu}_j^k$ are the j-th pixels in the phantom and the reconstruction from the k-th noise trial, respectively. For N_j in (4) and (20), we used a 3×3 local neighborhood for each pixel j, which yielded the maximum value of 9 for the center weight ω. Fig. 4 shows the contour plot for the MPEs of the PL-WMR reconstructions obtained with the 55 different pairs

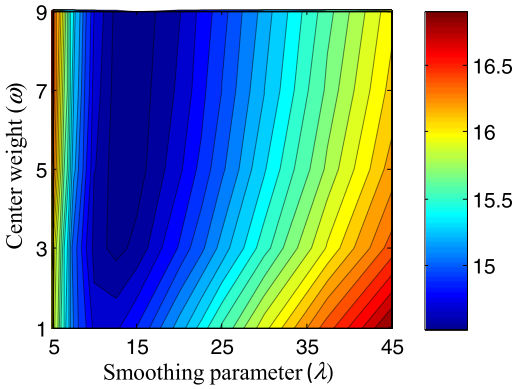

FIGURE 4. Contour plot for percentage errors (calculated from 50 independent noise trials) of PL-WMR reconstructions obtained with 55 different pairs of the smoothing parameter and the center weight.

of the smoothing parameter λ and center weight ω, where λ was set to the eleven different values of 5, 7.5, 10, 12.5, 15, 20, 22.5, 25, 30, 37.5 and 45, and ω was set to the five different values of 1, 3, 5, 7 and 9. In Fig. 4, PL-WMR yields the minimal value of MPE roughly when $\lambda \in (5, 25)$ and $\omega \in (3, 9]$, which indicates that, except for extremely low values of λ, increasing the center weight leads to the improved reconstructions in terms of MPE as compared to PL-WMR with $\omega = 1$ which is the standard MR.

Fig. 5 shows anecdotal PL reconstructions from the data shown in Fig. 2(b) using WMR, AWMR, WMR-AS, and AWMR-AS, where the value of the smoothing parameter for each reconstruction algorithm was set within the range of $\lambda \in (5, 25)$ according to the result in Fig. 4. For WMR, the value of ω was set to the three different values of 1, 5 and 9, and the value of λ was set to the three different values of 7.5, 15 and 22.5. (See Figs. 5(a), (b) and (c) for $\lambda = 7.5$, $\omega = 1$, 5 and 9, respectively, Figs. 5(e), (f) and (g) for $\lambda = 15$, $\omega = 1$, 5 and 9, respectively, and Figs. 5(i), (j) and (k) for $\lambda = 22.5$, $\omega = 1$, 5 and 9, respectively.) For AWMR, the value of ω was adaptively chosen within the range of $\omega \in [1, 9]$ and the smoothing parameter λ was set to the three different values of 7.5, 15 and 22.5. (See Figs. 5(d), (h) and (l) for $\omega = 1$, 5 and 9, respectively.) In this work, to avoid exhaustive search for the smoothing parameter, η in (14) was set to 0.5. For PL using WMR-AS in Figs. 5(m), (n) and (o), the value of ω was set to the three different values of 1, 5 and 9, respectively, and λ was adaptively chosen within the range of $\lambda \in [7.5, 22.5]$. For AWMR-AS in Fig. 5(p), both ω and λ were adaptively selected within the ranges of $\omega \in [1, 9]$ and $\lambda \in [7.5, 22.5]$, respectively.

The results shown in Figs. 5(a)(b)(c), (e)(f)(g) and (i)(j)(k) indicate that, as the center weight ω increases for a given value of λ, the WMR better captures the fine-scale edges, whereas it increases the roughness in the monotonic regions. This lies in the fact that the higher the value of ω, the lower the probability that the center pixel will be replaced by the neighbors, which is similar to the effect of decreasing the smoothing parameter λ so that the pixel to be updated is less affected by its neighbors.

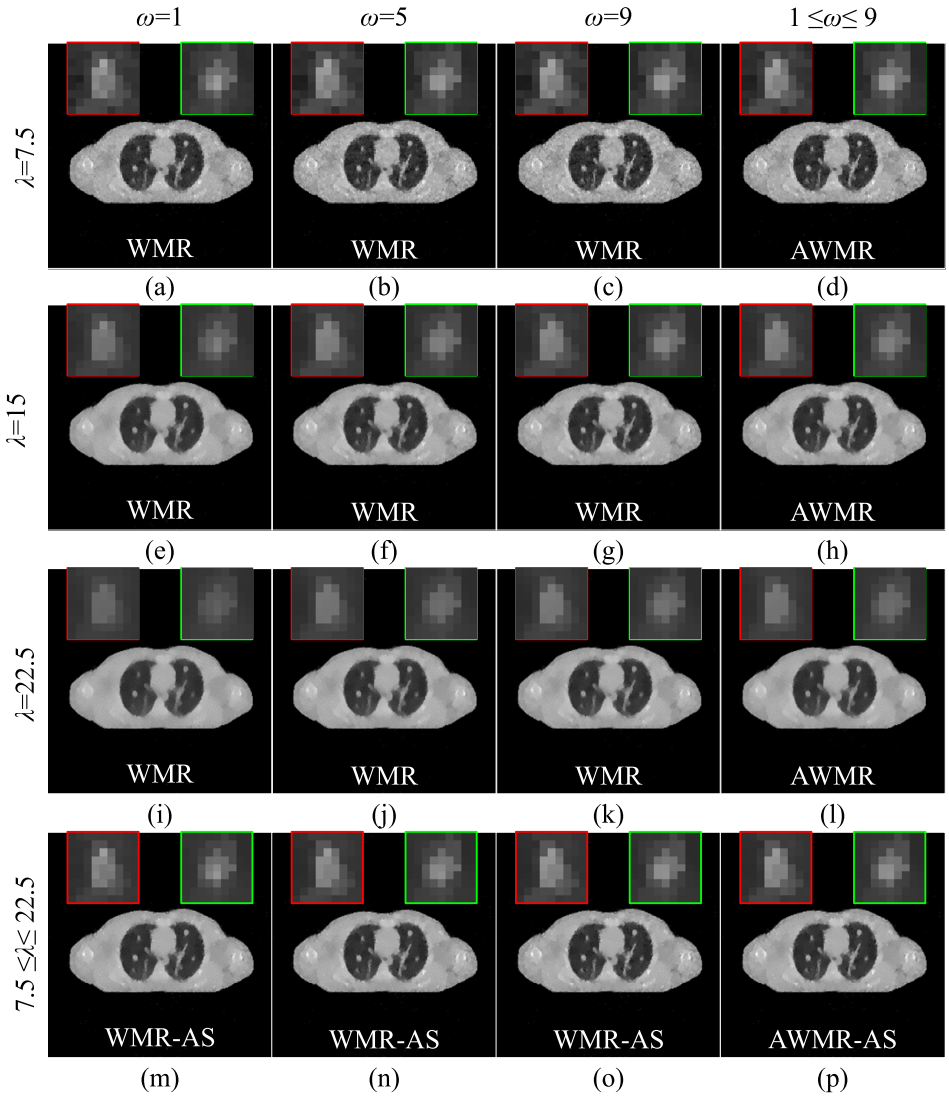

FIGURE 5. Anecdotal PL-WMR reconstructions from the transmission data shown in Fig. 2(b) using different values of the smoothing parameter λ and the center weight ω, (a) WMR with $\lambda = 7.5$ and $\omega = 1$ (PE = 14.765%), (b) WMR with $\lambda = 7.5$ and $\omega = 5$ (PE = 14.900%), (c) WMR with $\lambda = 7.5$ and $\omega = 9$ (PE = 15.045%), (d) AWMR with $\lambda = 7.5$ (PE = 14.718%), (e) WMR with $\lambda = 15$ and $\omega = 1$ (PE = 14.607%), (f) WMR with $\lambda = 15$ and $\omega = 5$ (PE = 14.247%), (g) WMR with $\lambda = 15$ and $\omega = 9$ (PE = 14.225%), (h) AWMR with $\lambda = 15$ (PE = 14.242%), (i) WMR with $\lambda = 22.5$ and $\omega = 1$ (PE = 15.169%), (j) WMR with $\lambda = 22.5$ and $\omega = 5$ (PE = 14.629%), (k) WMR with $\lambda = 22.5$ and $\omega = 9$ (PE = 14.523%), (l) AWMR with $\lambda = 22.5$ (PE = 14.666%), (m) WMR-AS with $\omega = 1$ (PE = 14.351%), (n) WMR-AS with $\omega = 5$ (PE = 14.156%), (o) WMR-AS with $\omega = 9$ (PE = 14.125%), (p) AWMR-AS (PE = 14.116%).

On the other hand, for a given value of the smoothing parameter, the AWMR adaptively selects the value of the center weight. Figs. 5(d), (h) and (l) compared with Figs. 5(c), (g) and (k), respectively, indicate that, the AWMR not only preserves the fine-scale edges just like the WMR with $\omega = 9$, but also better suppresses the noise in monotonic regions than the WMR with $\omega = 9$.

Note that, for a given value of the smoothing parameter, the PEs of AWMR in Figs. 5(d), (h) and (l) are close to those of WMR with $\omega = 5$ in Figs. 5(b), (f) and (j). Similarly, for a given value of the center weight, the PEs of WMR-AS in Figs. 5(m), (n) and (o) are similar to those of WMR with $\lambda = 15$ in Fig. 5(e), (f) and (g). However, each of the WMR's adaptive versions (AWMR and WMR-AS) is still less than ideal due to its own limitation in simultaneously preserving edges and reducing noise. On the other hand, the combined AWMR and WMR-AS, namely the AWMR-AS, not only takes advantages of AWMR and WMR-AS in selecting the values of ω and λ, but also outperforms both methods in terms of PE.

As the AWMR-AS method requires an initial guess of the smoothing parameter λ, which is denoted as α in (14), to determine the proper range of λ, we attempted to observe the effect of λ over a range by measuring

the MPEs defined in (21) from 50 independent noise trials.

Fig. 6(a) shows the MPE curves versus the smoothing parameter λ for PL reconstructions using WMR with $\omega = 1$, 5 and 9, and AWMR, where each curve was measured from the results calculated from the eleven different values of λ within the range of $\lambda \in [5, 45]$ for each reconstruction algorithm. Similarly, Fig. 6(b) shows the MPE curves for PL using WMR-AS with $\omega = 1$, 5 and 9, and AWMR-AS. Note that each MPE value was designated at the center value of λ (10, 15, 20, 25 and 30) in (14) within each range of λ ([5,15], [7.5,22.5], [10,30], [12.5,37.5] and [15,45], respectively).

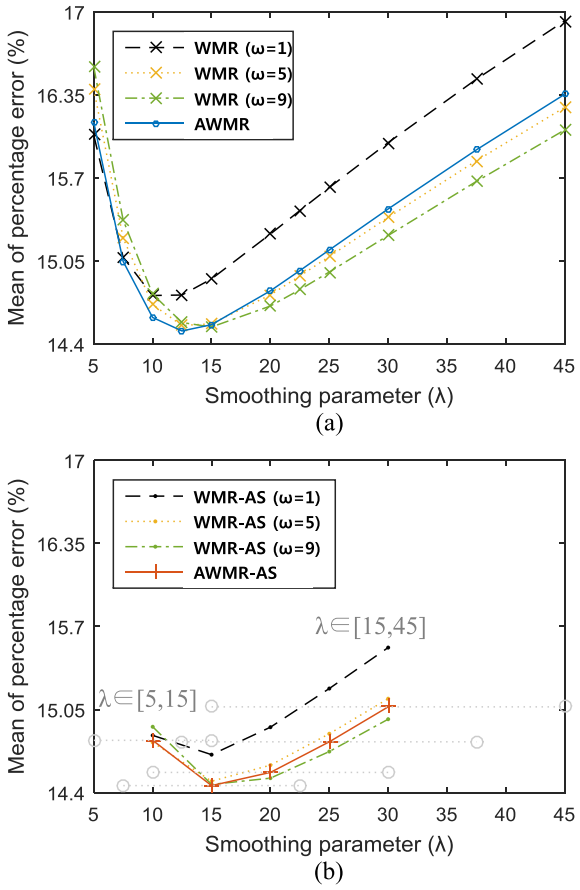

FIGURE 6. Mean of percentage error (calculated from 50 independent noise trials) versus smoothing parameter curves for PL using WMR (ω = 1, 5, 9), AWMR, WMR-AS (ω = 1, 5, 9) and AWMR-AS, (a) WMR (ω = 1, 5, 9) and AWMR, (b) WMR-AS (ω = 1, 5, 9) and AWMR-AS (Since the smoothing parameter in both WMR-AS and AWMR-AS is adaptively chosen for each pixel, its value is unknown. Therefore, each MPE value was designated at the center value of the smoothing parameter, i.e., 10, 15, 20, 25 and 30.)

According to Fig. 6(a), the overall MPEs for AWMR are much smaller than those for WMR with $\omega = 1$ and comparable to those for WMR with $\omega = 5$. On the other hand, Fig. 6(b) shows that, by adaptively selecting the smoothing parameter at each pixel, the range of each MPE curve is relatively smaller than that of each MPE curve shown in Fig. 6(a). Note that the ranges of λ for WMR-AS and AWMR-AS are the same as those for WMR and AWMR. Note also that AWMR-AS with $\lambda \in [7.5, 22.5]$ outperforms other algorithms in terms of MPE.

To validate our proposed methods more quantitatively, we conducted regional studies using the contrast recovery coefficient (CRC) [56] which represents the degree of the recovered contrast of a region relative to the background region. The CRC in each region of interest (ROI) is defined as

$$CRC_{\Re}^{k} = \frac{CR_{\Re}^{k}}{CR_{\Re}^{0}}, \quad \text{where } CR_{\Re}^{k} = \frac{\left|Z_{\Re}^{k} - Z_{\mathrm{B}}^{k}\right|}{Z_{\mathrm{B}}^{k}}. \tag{22}$$

In (22), $CR_{\Re}^{0}$ is the true contrast in the phantom, Z_{B}^{k} is the mean attenuation in the background region, and $Z_{\Re}^{k}$ represents the mean attenuation in each ROI $\Re$ at the k-th noise trial, i.e., $Z_{\Re}^{k} = \sum_{j\in\Re}\left(\hat{\mu}_{j}^{k} \Big/ u_{\Re}\right)$, where $u_{\Re}$ is the number of pixels in each ROI. The ensemble mean of CRC is then defined as

$$\overline{CRC}_{\Re} = \frac{1}{K}\sum_{k=1}^{K} CRC_{\Re}^{k}. \tag{23}$$

The ensemble mean of the background SD is calculated by

$$\bar{\sigma}_{\mathrm{B}} = \frac{1}{K}\sum_{k=1}^{K}\sigma_{\mathrm{B}}^{k},$$

$$\text{where} \quad \sigma_{\mathrm{B}}^{k} = \sqrt{\frac{1}{u_{\mathrm{B}}-1}\sum_{j\in\mathrm{B}}\left[\hat{\mu}_{j}^{k} - \left(\frac{1}{u_{\mathrm{B}}}\sum_{j'\in\mathrm{B}}\hat{\mu}_{j'}^{k}\right)\right]^{2}}. \tag{24}$$

In (24), u_{B} is the number of pixels in pre-selected background region B.

Fig. 7(a) shows the pre-selected four regions (R_1, R_2, R_3 and R_4) containing edges and a background region located in the dark area. Note that the background SD on the abscissa is not the SD of the background region for the CRCs but is the SD of a background region to measure the noise level of each reconstruction, which is not shown in Fig. 7(a).

Figs. 7(b), (c), (d) and (e) show the ensemble mean (calculated from 50 independent noise trials) of the regional CRC versus the background SD curves for the PL using WMR with $\omega = 1$, 5 and 9, AWMR, WMR-AS with $\omega = 1$, 5 and 9, and AWMR-AS, where each CRC-SD curve for the WMR with $\omega = 1$, 5 and 9, and AWMR includes the results from the eleven different values of λ within the range of $\lambda \in [5, 45]$. For WMR-AS with $\omega = 1$, 5 and 9, and AWMR-AS, each CRC-SD curve was measured from the results with the smoothing parameter adaptively selected at each pixel within the ranges of $\lambda \in [5, 15]$, [7.5, 22.5], [10, 30], [12.5, 37.5] and [15, 45] centered at $\lambda = 10$, 15, 20, 25 and 30, respectively.

According to the results from the ROI studies, WMR with $\omega = 9$ yields relatively high CRCs only when its background SDs are very high. This indicates that setting the center weight for WMR to a larger value allows the algorithm to provide the higher regional contrast but yields unfortunate

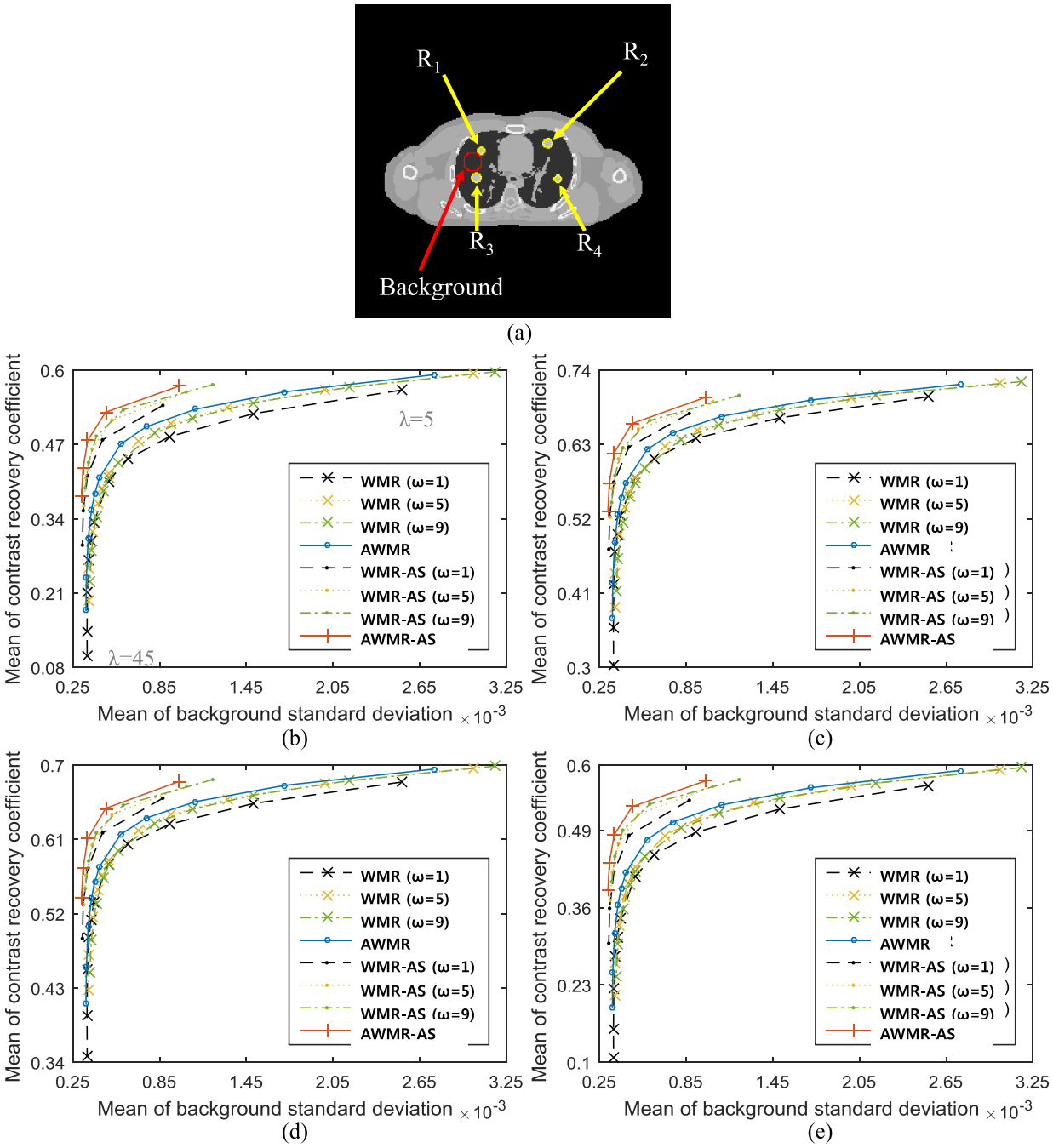

FIGURE 7. Mean of regional contrast recovery coefficient versus mean of background standard deviation (calculated from 50 independent noise trials) curves for PL using WMR (ω = 1, 5, 9), AWMR, WMR-AS (ω = 1, 5, 9) and AWMR-AS, (a) ROIs for regional contrast recovery coefficient, (b) results for R_1, (c) results for R_2, (d) results for R_3, (e) results for R_4.

effect of degrading the performance of noise suppression in the locally monotonic regions. In contrast, the AWMR overcomes this limitation due to the trade-off between CRC and background SD by adaptively choosing the value of the center weight ω_{jj} at each pixel. Similarly, as the smoothing parameter λ_j is adaptively adjusted, the limitation of WMR due to the trade-off between the CRC and background SD can be overcome. Finally, AWMR-AS further improves WMR-AS and achieves the exceptional performance in the regional contrast recovery while maintaining relatively low background SDs.

V. SUMMARY AND CONCLUSION

We have developed a new method of adaptively selecting the weight for the center-weighted median regularizer in PL reconstruction for TCT. Our method of using the

cumulative histogram of the SD image has the effect of enhancing the fine-scale edges by boosting up the center weights of the pixels with relatively low SD values. Transforming each pixel of the SD image into the center weight via the NCH curve is equivalent to transforming each pixel of the histogram-equalized SD image into the center weight. With the histogram-equalized SD image, the AWMR can preserve edges with low SD values as well as edges with high SD values. According to our simulation results, for all levels of the smoothing parameter, the accuracies of the AWMR results in terms of MPE were comparable to or even better in some cases than those of the best WMR results with the manually chosen center weights.

We have also tested the similar method of adaptively selecting the optimal value of the smoothing parameter for each pixel using the flipped NCH curve that transforms the high pixel values of the histogram-equalized SD image into the low values of the smoothing parameter, and vice versa. Our experimental results indicate that, when the smoothing parameter is adaptively chosen for each pixel in AWMR, which is referred to as AWMR-AS, the performance is improved further in terms of the ensemble mean of regional CRC as well as the MPE. Although WMR can generate better results than AWMR or AWMR-AS for some particular combinations of the center weight and smoothing parameter, it does not guarantee reliable results with equally good image qualities for different objects.

The net conclusion is that our PL algorithm using AWMR or AWMR-AS is more practical and reliable than other median-based regularization methods, such as the methods proposed in [33], [35], in that it is not only derived completely as the minimization of a joint convex objective dedicated to TCT, but also alleviates the difficulty in judicious choices of hyperparameters, such as the median center weight and the smoothing parameter.

REFERENCES

[1] A. C. Kak and M. Slaney, *Principles Of Computerized Tomographic Imaging*. New York, NY, USA: IEEE Press, 1988.

[2] G. T. Herman, *Image Reconstruction from Projections*. New York, NY, USA: Academic, 1980.

[3] K. J. Batenburg and J. Sijbers, "DART: A practical reconstruction algorithm for discrete tomography," *IEEE Trans. Image Process.*, vol. 20, no. 9, pp. 2542–2553, Sep. 2011.

[4] J. Hsieh, B. Nett, Z. Yu, K. Sauer, J.-B. Thibault, and C. A. Bouman, "Recent advances in CT image reconstruction," *Current Radiol. Rep.*, vol. 1, no. 1, pp. 39–51, Mar. 2013.

[5] L. Lu and B. Honours, "Model-based iterative reconstruction: A promising algorithm for today's computed tomography imaging," *J. Med. Imag. Radiat. Sci.*, vol. 45, pp. 131–136, Jun. 2014.

[6] K. Lange and R. Carson, "EM reconstruction algorithms for emission and transmission tomography," *J. Comput. Assist. Tomogr.*, vol. 8, no. 2, pp. 306–316, Apr. 1984.

[7] C. Bouman and K. Sauer, "A generalized Gaussian image model for edge-preserving MAP estimation," *IEEE Trans. Image Process.*, vol. 2, no. 3, pp. 296–310, Jul. 1993.

[8] E. U. Mumcuoglu, R. Leahy, S. R. Cherry, and Z. Zhou, "Fast gradient-based methods for Bayesian reconstruction of transmission and emission PET images," *IEEE Trans. Med. Imag.*, vol. 13, no. 4, pp. 687–701, Dec. 1994.

[9] K. Lange and J. A. Fessler, "Globally convergent algorithms for maximum a posteriori transmission tomography," *IEEE Trans. Image Process.*, vol. 4, no. 10, pp. 1430–1438, Oct. 1995.

[10] S.-J. Lee, A. Rangarajan, and G. Gindi, "Bayesian image reconstruction in SPECT using higher order mechanical models as priors," *IEEE Trans. Med. Imag.*, vol. 14, no. 4, pp. 669–680, Dec. 1995.

[11] M. T. Chan, G. T. Herman, and E. Levitan, "A Bayesian approach to PET reconstruction using image-modeling gibbs priors: Implementation and comparison," *IEEE Trans. Nucl. Sci.*, vol. 44, no. 3, pp. 1347–1354, Jun. 1997.

[12] I.-T. Hsiao, A. Rangarajan, and G. Gindi, "Joint-MAP Bayesian tomographic reconstruction with a gamma-mixture prior," *IEEE Trans. Image Process.*, vol. 11, no. 12, pp. 1466–1477, Dec. 2002.

[13] J. Nuyts and J. A. Fessler, "A penalized-likelihood image reconstruction method for emission tomography, compared to postsmoothed maximum-likelihood with matched spatial resolution," *IEEE Trans. Med. Imag.*, vol. 22, no. 9, pp. 1042–1052, Sep. 2003.

[14] C. Kamphius and F. J. Beekman, "Accelerated iterative transmission CT reconstruction using an ordered subsets convex algorithm," *IEEE Trans. Med. Imag.*, vol. 17, no. 6, pp. 1001–1005, Dec. 1998.

[15] H. Erdogan and J. A. Fessler, "Ordered subsets algorithms for transmission tomography," *Phys. Med. Biol.*, vol. 44, no. 11, pp. 2835–2851, Nov. 1999.

[16] S.-J. Lee, "Accelerated deterministic annealing algorithms for transmission CT reconstruction using ordered subsets," *IEEE Trans. Nucl. Sci.*, vol. 49, no. 5, pp. 2373–2380, Oct. 2002.

[17] P. Després and X. Jia, "A review of GPU-based medical image reconstruction," *Phys. Medica*, vol. 42, pp. 76–92, Oct. 2017.

[18] J. S. Kole and F. J. Beekman, "Evaluation of accelerated iterative X-ray CT image reconstruction using floating point graphics hardware," *Phys. Med. Biol.*, vol. 51, no. 4, pp. 875–889, Feb. 2006.

[19] M. G. McGaffin and J. A. Fessler, "Alternating dual updates algorithm for X-ray CT reconstruction on the GPU," *IEEE Trans. Comput. Imag.*, vol. 1, no. 3, pp. 186–199, Sep. 2015.

[20] P. J. Green, "Bayesian reconstructions from emission tomography data using a modified EM algorithm," *IEEE Trans. Med. Imag.*, vol. 9, no. 1, pp. 84–93, Mar. 1990.

[21] K. Lange, "Convergence of EM image reconstruction algorithms with Gibbs smoothing," *IEEE Trans. Med. Imag.*, vol. 9, no. 4, pp. 439–446, 1990.

[22] S.-J. Lee, "Performance comparison of convex-nonquadratic priors for Bayesian tomographic reconstruction," *J. Electron. Imag.*, vol. 9, no. 3, pp. 242–250, 2000.

[23] A. Buades, B. Coll, and J. M. Morel, "A review of image denoising algorithms, with a new one," *Multiscale Model. Simul.*, vol. 4, no. 2, pp. 490–530, Jan. 2005.

[24] V.-G. Nguyen and S.-J. Lee, "Incorporating anatomical side information into PET reconstruction using nonlocal regularization," *IEEE Trans. Image Process.*, vol. 22, no. 10, pp. 3961–3973, Oct. 2013.

[25] Z. Tian, X. Jia, B. Dong, Y. Lou, and S. B. Jiang, "Low-dose 4DCT reconstruction via temporal nonlocal means," *Med. Phys.*, vol. 38, no. 3, pp. 1359–1365, Feb. 2011.

[26] H. Zhang, D. Zeng, H. Zhang, J. Wang, Z. Liang, and J. Ma, "Applications of nonlocal means algorithm in low-dose X-ray CT image processing and reconstruction: A review," *Med. Phys.*, vol. 44, no. 3, pp. 1168–1185, Mar. 2017.

[27] X. Ren and S.-J. Lee, "Image reconstruction for emission tomography using intensity normalised patch-based regularisation," *IET Image Process.*, vol. 13, no. 5, pp. 794–803, Apr. 2019.

[28] G. Wang and J. Qi, "Penalized likelihood PET image reconstruction using patch-based edge-preserving regularization," *IEEE Trans. Med. Imag.*, vol. 31, no. 12, pp. 2194–2204, Dec. 2012.

[29] H. Chen, Y. Zhang, W. Zhang, P. Liao, K. Li, J. Zhou, and G. Wang, "Low-dose CT via convolutional neural network," *Biomed. Opt. Express*, vol. 8, no. 2, pp. 679–694, 2017.

[30] K. H. Jin, M. T. McCann, E. Froustey, and M. Unser, "Deep convolutional neural network for inverse problems in imaging," *IEEE Trans. Image Process.*, vol. 26, no. 9, pp. 4509–4522, Sep. 2017.

[31] K. Gong, J. Guan, K. Kim, X. Zhang, J. Yang, Y. Seo, G. El Fakhri, J. Qi, and Q. Li, "Iterative PET image reconstruction using convolutional neural network representation," *IEEE Trans. Med. Imag.*, vol. 38, no. 3, pp. 675–685, Mar. 2019.

[32] S. Alenius and U. Ruotsalainen, "Bayesian image reconstruction for emission tomography based on median root prior," *Eur. J. Nucl. Med.*, vol. 24, no. 3, pp. 258–265, Mar. 1997.

[33] S. Alenius and U. Ruotsalainen, "Generalization of median root prior reconstruction," *IEEE Trans. Med. Imag.*, vol. 21, no. 11, pp. 1413–1420, Nov. 2002.
[34] I.-T. Hsiao, A. Rangarajan, and G. Gindi, "A new convex edge-preserving median prior with applications to tomography," *IEEE Trans. Med. Imag.*, vol. 22, no. 5, pp. 580–585, May 2003.
[35] Y. Liu, H. Shangguan, Q. Zhang, H. Zhu, H. Shu, and Z. Gui, "Median prior constrained TV algorithm for sparse view low-dose CT reconstruction," *Comput. Biol. Med.*, vol. 60, pp. 117–131, May 2015.
[36] S.-J. Ko and Y. H. Lee, "Center weighted median filters and their applications to image enhancement," *IEEE Trans. Circuits Syst.*, vol. 38, no. 9, pp. 984–993, 1991.
[37] T. Sun, M. Gabbouj, and Y. Neuvo, "Center weighted median filters: Some properties and their applications in image processing," *Signal Process.*, vol. 35, no. 3, pp. 213–229, Feb. 1994.
[38] T. Chen and H. R. Wu, "Adaptive impulse detection using center-weighted median filters," *IEEE Signal Process. Lett.*, vol. 8, no. 1, pp. 1–3, Jan. 2001.
[39] L. Yin, R. Yang, M. Gabbouj, and Y. Neuvo, "Weighted median filters: A tutorial," *IEEE Trans. Circuits Syst. II, Analog Digit. Signal Process.*, vol. 43, no. 3, pp. 157–192, Mar. 1996.
[40] G. R. Arce, "A general weighted median filter structure admitting negative weights," *IEEE Trans. Signal Process.*, vol. 46, no. 12, pp. 3195–3205, 1998.
[41] Y. Dong and S. Xu, "A new directional weighted median filter for removal of random-valued impulse noise," *IEEE Signal Process. Lett.*, vol. 14, no. 3, pp. 193–196, Feb. 2007.
[42] J. Chen, Y. Zhan, and H. Cao, "Adaptive sequentially weighted median filter for image highly corrupted by impulse noise," *IEEE Access*, vol. 7, pp. 158545–158556, 2019.
[43] T. C. Aysal and K. E. Barner, "Generalized mean-median filtering for robust frequency-selective applications," *IEEE Trans. Signal Process.*, vol. 55, no. 3, pp. 937–948, Mar. 2007.
[44] Y. Li and G. R. Arce, "A maximum likelihood approach to least absolute deviation regression," *EURASIP J. Adv. Signal Process.*, vol. 2004, no. 12, pp. 1762–1769, Dec. 2004.
[45] J. A. Fessler and W. L. Rogers, "Spatial resolution properties of penalized-likelihood image reconstruction: Space-invariant tomographs," *IEEE Trans. Image Process.*, vol. 5, no. 9, pp. 1346–1358, Sep. 1996.
[46] S. Z. Li, "Close-form solution and parameter selection for convex minimization-based edge-preserving smoothing," *IEEE Trans. Pattern Anal. Mach. Intell.*, vol. 20, no. 9, pp. 916–932, Sep. 1998.
[47] J. Qi and R. M. Leahy, "Resolution and noise properties of MAP reconstruction for fully 3-D PET," *IEEE Trans. Med. Imag.*, vol. 19, no. 5, pp. 493–506, May 2000.
[48] S.-J. Lee, "Training set approach to smoothing parameter estimation for spline-regularized tomographic reconstruction," *Opt. Eng.*, vol. 48, no. 2, Feb. 2009, Art. no. 027003.
[49] M. Zhang, J. Zhou, X. Niu, E. Asma, W. Wang, and J. Qi, "Regularization parameter selection for penalized-likelihood list-mode image reconstruction in PET," *Phys. Med. Biol.*, vol. 62, no. 12, pp. 5114–5130, Jun. 2017.
[50] S. Ahn, J. A. Fessler, D. Blatt, and A. O. Hero, "Convergent incremental optimization transfer algorithms: Application to tomography," *IEEE Trans. Med. Imag.*, vol. 25, no. 3, pp. 283–296, Mar. 2006.
[51] Z. Yu, J.-B. Thibault, C. A. Bouman, K. D. Sauer, and J. Hsieh, "Fast model-based X-ray CT reconstruction using spatially nonhomogeneous ICD optimization," *IEEE Trans. Image Process.*, vol. 20, no. 1, pp. 161–175, Jan. 2011.
[52] D. Kim, S. Ramani, and J. A. Fessler, "Combining ordered subsets and momentum for accelerated X-ray CT image reconstruction," *IEEE Trans. Med. Imag.*, vol. 34, no. 1, pp. 167–178, Jan. 2015.
[53] H. M. Hudson and R. S. Larkin, "Accelerated image reconstruction using ordered subsets of projection data," *IEEE Trans. Med. Imag.*, vol. 13, no. 4, pp. 601–609, Dec. 1994.
[54] A. R. De Pierro, "A modified expectation maximization algorithm for penalized likelihood estimation in emission tomography," *IEEE Trans. Med. Imag.*, vol. 14, no. 1, pp. 132–137, Mar. 1995.
[55] W. P. Segars, G. Sturgeon, S. Mendonca, J. Grimes, and B. M. W. Tsui, "4D XCAT phantom for multimodality imaging research," *Med. Phys.*, vol. 37, no. 9, pp. 4902–4915, Aug. 2010.
[56] J.-S. Liow and S. C. Strother, "Practical tradeoffs between noise, quantitation, and number of iterations for maximum likelihood-based reconstructions," *IEEE Trans. Med. Imag.*, vol. 10, no. 4, pp. 563–571, Dec. 1991.

JI EUN JUNG received the B.S. and M.S. degrees in electronic engineering from Pai Chai University, Daejeon, South Korea, in 2013 and 2015, respectively, and the Ph.D. degrees in electronic engineering from Pai Chai University and in computer science and electrical engineering from Kumamoto University, Kumamoto, Japan, in 2019. She is currently a Technical Staff Member with the Image Processing Group, Genoray Company Ltd., Seongnam, South Korea. Her research interests include image processing and medical imaging. In particular, she is interested in image reconstruction for X-ray computed tomography.

SOO-JIN LEE (Senior Member, IEEE) received the B.S. and M.S. degrees in electronic engineering from Sogang University, Seoul, South Korea, in 1984 and 1986, respectively, and the Ph.D. degree in electrical engineering from Stony Brook University, Stony Brook, NY, USA, in 1995. From 1986 to 1991, he was a Research Staff Member with LG Electronics Company Ltd., Anyang, South Korea, working on the development of magnetic resonance imaging systems. In 1995, he was a Postdoctoral Research Associate with the Department of Radiology, Stony Brook University. He was a Senior Research Scientist with the Korea Institute of Science and Technology, Seoul, in 1996. In 1997, he joined the Faculty of Pai Chai University, Daejeon, South Korea, where he is currently a Professor of Electronic Engineering. From 2004 to 2005, he was a Visiting Associate Professor with the Department of Molecular and Medical Pharmacology, University of California at Los Angeles, Los Angeles, CA, USA. His current research interests include computational imaging and image processing with an emphasis on the tomographic reconstruction problem.